



# Unsteady boundary-layer transition measurements and computations on a rotating blade under cyclic pitch conditions

Armin Weiss<sup>1</sup> · C. Christian Wolf<sup>1</sup> · Kurt Kaufmann<sup>1</sup> · Johannes N. Braukmann<sup>1</sup> · James T. Heineck<sup>2</sup> · Markus Raffel<sup>1</sup>

Received: 30 July 2019 / Revised: 27 November 2019 / Accepted: 24 January 2020  
© The Author(s) 2020

## Abstract

The presented work tackles the lack of experimental investigations of unsteady laminar-turbulent boundary-layer transition on rotor blades at cyclic pitch actuation, which are important for accurate performance predictions of helicopters in forward flight. Unsteady transition positions were measured on the blade suction side of a four-bladed subscale rotor by means of non-intrusive differential infrared thermography (DIT). Experiments were conducted at different rotation rates corresponding to Mach and Reynolds numbers at 75% rotor radius of up to  $M_{75} = 0.21$  and  $Re_{75} = 3.3 \times 10^5$  and with varying cyclic blade pitch settings. The setup allowed transition to be measured across the outer 54% of the rotor radius. For comparison, transition was also measured using conventional infrared thermography for steady cases with collective pitch settings only. The study is complemented by numerical simulations including boundary-layer transition modeling based on semi-empirical criteria. DIT results reveal the upstream and downstream motion of boundary-layer transition during upstroke and downstroke, a reasonable comparison to experimental results obtained using the already established  $\sigma_{c_p}$  method, and noticeable agreement with numerical simulations. The result is the first systematic study of unsteady boundary-layer transition on a rotor suction side by means of DIT including a comparison to numerical computations.

## Abbreviations

AHD	Boundary-layer transition criterion according to Arnal, Habiballah and Delcourt
CFD	Computational fluid dynamics
DIT	Differential infrared thermography
DLR	German Aerospace Center
IR	Infrared
NASA	National Aeronautics and Space Administration
ONERA	The French Aerospace Lab
RTG	Rotor test facility of the DLR in Göttingen
RBT	Rotor blade transition
TAU	Unstructured finite-volume CFD code

TS	Tollmien–Schlichting
SLS	Strained-Layer supperlattice

## List of symbols

$A_{\text{blades}}$	Blade planform area, $A_{\text{blades}} = 2cR$
$c$	Chord length, $c = 0.072 \text{ m}$
$c_l$	Sectional lift coefficient, $c_l = (\text{lift}/1 \text{ m}) / \left[ \frac{\rho_\infty}{2} \cdot (2\pi r f_{\text{rotor}})^2 \cdot c \right]$
$C_T/\sigma$	Blade loading coefficient
$f_{\text{rotor}}$	Rotation frequency of rotor, Hz
$f_{\text{mirror}}$	Rotation frequency of rotating mirror, Hz
$F_{\text{thrust}}$	Thrust force, N
$I_{\text{pos 1 2}}$	Image gray levels at pos 1 or pos 2, counts
$\Delta I_{\text{DIT}}$	DIT signal, counts
$k$	Turbulent kinetic energy, $\text{m}^2/\text{s}^2$
$k_{75}$	Reduced frequency, $k_{75} = c/(2 \cdot 0.75 R)$
$M_{75}$	Mach number based on $2\pi f_{\text{rotor}} \cdot 0.75R$
pos 1 2	Azimuth positions at image acquisition
$r$	Coordinate in radial direction, m
$R$	Rotor radius, $R = 0.650 \text{ m}$
$Re_{75}$	Chord Reynolds number, based on $2\pi f_{\text{rotor}} \cdot 0.75R$
$t$	Time, s
$T_\infty$	Total temperature in test section, K
$t/T$	Phase of pitch cycle, $t/T = t f_{\text{rotor}}'$
$Tu$	Turbulence intensity
$U_{\text{loc}}$	Local flow velocity, m/s

This work was conducted within the framework of the DLR project “FAST-Rescue”. James Heineck’s participation was accommodated under the NASA-DLR Memorandum of Understanding Implementing Arrangement for Experimental Optical Methods Applied to Helicopter Research.

✉ Armin Weiss  
armin.weiss@dlr.de

<sup>1</sup> Institute of Aerodynamics and Flow Technology, German Aerospace Center, DLR, Bunsenstr. 10, 37073 Göttingen, Germany

<sup>2</sup> NASA Ames Research Center, Moffett Field, Mountain View, California 94035, USA

$x$	Coordinate in chordwise direction, m
$v_\infty$	Wind tunnel flow velocity, m/s
$\beta$	Angle between rotor axis and axis of rotating mirror, °
$\Theta_{75}$	Blade pitch angle at $r/R = 0.75$ , °
$\bar{\Theta}_{75}$	Collective pitch angle at $r/R = 0.75$ , °
$\hat{\Theta}$	Amplitude of cyclic pitch setting, °
$\rho_\infty$	Density, kg/m <sup>3</sup>
↑	Upstroke, increasing pitch angle
↓	Downstroke, decreasing pitch angle

## 1 Introduction

Laminar-turbulent boundary-layer transition strongly affects the power requirement of helicopter rotors. Numerical simulations of rotor aerodynamics often do not consider boundary-layer transition. This is due to a lack of appropriate transition models, which must account for the complex three-dimensional and unsteady flow conditions of a rotor in forward flight, and therefore need experimental data for validation.

Measurements of unsteady boundary-layer transition on rotor blades for the validation of transition models are a challenging task. Many experiments reduce the complexity of a rotor setup by investigating boundary-layer transition on periodically pitching airfoils equipped with locally installed fast-response hot-film sensors (Lorber and Carta 1992) or dynamic pressure transducers (Gardner and Richter 2015). The application of these techniques in the rotating frame demands the laborious effort of integrating the sensor into the model, yields results at only discrete locations, and possibly disturbs the boundary-layer flow. The techniques have been demonstrated in experiments using hot-film sensors integrated into the blades of a subscale helicopter model (Raffel et al. 2011), or pressure transducers in dynamically pitching Mach-scaled rotor blades (Schwermer et al. 2019).

Infrared (IR) imaging is well-established to detect boundary-layer transition in steady aerodynamics, such as on rotor blades in hover (Overmeyer and Martin 2017) or climb (Weiss et al. 2017) conditions. Differential infrared thermography (DIT) is a non-intrusive optical alternative to locally blade-mounted sensors for the detection of unsteady boundary-layer transition. The basic idea is to subtract two infrared images taken with a short time delay in order to detect the intermediate transition motion. Raffel and Merz (2014) have demonstrated the measurement principle in proof-of-concept experiments, Richter et al. (2016) validated the technique against hot-films and dynamic pressure sensors, and Wolf et al. (2019) optimized DIT for various experimental conditions.

Recently, Overmeyer et al. (2018) applied DIT to the pressure side of a large-scale model rotor in forward flight conditions, showing promising results. Nevertheless, some questions regarding the interpretation of results remain unanswered, most probably due to the influence of the azimuthally varying stagnation temperature of the flow. Gardner et al. (2019b) investigated boundary-layer transition on the rotor blade suction side of a full-scale EC135 helicopter in forward flight by means of DIT. Due to the challenging experimental setup, e.g., the varying and large distance between the observation helicopter and the test object during formation flight, only a few data points indicating boundary-layer transition have been presented. To the authors knowledge, a systematic experimental study of unsteady boundary-layer transition on a helicopter rotor at cyclic pitch is still missing.

Current approaches to boundary-layer-transition modeling for computational fluid dynamics (CFD) codes face difficult challenges when implemented into rotating systems. Recent activities focused on boundary-layer transition computations of NASA's 'PSP-rotor' experiment in hover (see Coder 2017; Vieira et al. 2017; Parwani and Coder 2018; Zhao et al. 2018) and forward flight (Carnes and Coder 2019), as well as on the S-76 rotor in hover (Min et al. 2018).

Investigations at the German Aerospace Center (DLR) and at the French Aerospace Lab (ONERA) have shown that approximate transition modeling in unsteady Reynolds-averaged Navier–Stokes simulations can provide an improved prediction of the rotor performance in hover (Heister 2012; Richez et al. 2017) and forward flight (Richez et al. 2017; Heister 2018) when using relatively coarse grids, which are especially applicable to industrial aircraft development efforts. The GOAHEAD data set (Raffel et al. 2011) was used for validation but the available hot-film data are too sparsely sampled to provide reliable validation of the codes.

In the framework of a DLR-ONERA cooperation, Kaufmann et al. (2019) performed boundary-layer-transition computations that have shown promising results when compared to experimental data sets obtained on a two-bladed Mach-scaled rotor under collective (Weiss et al. 2017) and cyclic (Schwermer et al. 2019) pitch conditions in the Rotor Test Facility at DLR Göttingen (RTG, Schwermer et al. 2016). Still, the computations of the cyclic test case showed the need for spatially highly resolved measurements of unsteady boundary-layer transition.

In this paper, unsteady boundary-layer transition is investigated on the four-bladed subscale model rotor of the well-instrumented RTG. The experiments include a variation of cyclic blade pitch angles at different rotation frequencies as well as cases with only collective pitch settings. Two of the main objectives are to evaluate the feasibility of DIT measurements under rotor conditions

and to investigate the effect of different pitch rates on unsteady boundary-layer transition positions by independent variation of pitch amplitude and frequency. Measured data are further compared to unsteady boundary-layer transition computations using the DLR-TAU code and the rotor blade transition (RBT) tool as recently applied by Kaufmann et al. (2019) The result is the first systematic study of unsteady boundary-layer transition on a rotor suction side by means of DIT including a comparison to numerical prediction capabilities at DLR.

## 2 Experimental and numerical setup

### 2.1 Experimental setup

The experiments were conducted at the RTG (Schwermer et al. 2016) of the DLR in Göttingen. The four-bladed rotor (see Fig. 1) was placed into the test section of an Eiffel-type wind tunnel with a nozzle cross section of 1.6 m × 3.4 m. The rotor axis is horizontal and a slow axial inflow ( $v_\infty = 2.2$  and 4.9 m/s) was provided to prevent recirculation of tip vortices and blade-vortex interaction.

The rotor blades (see Fig. 2) were made out of carbon fiber reinforced plastic, had a radius of  $R = 0.650$  m, a chord length of  $c = 0.072$  m and a constant thickness ratio of 9% chord. The blades were equipped with the DSA-9A helicopter airfoil and comprised of a parabolic SPP8 tip without anhedral (see Vuillet et al. 1989), which started at 91% radius and led to a tip chord length of 0.024 m (see Schwermer et al. 2016). A negative linear twist of  $-9.33^\circ$  was incorporated along the blades' span between  $0.25 < r/R < 1$ . The investigated blade was equipped with fast-response pressure transducers at  $r/R = 0.53$  and

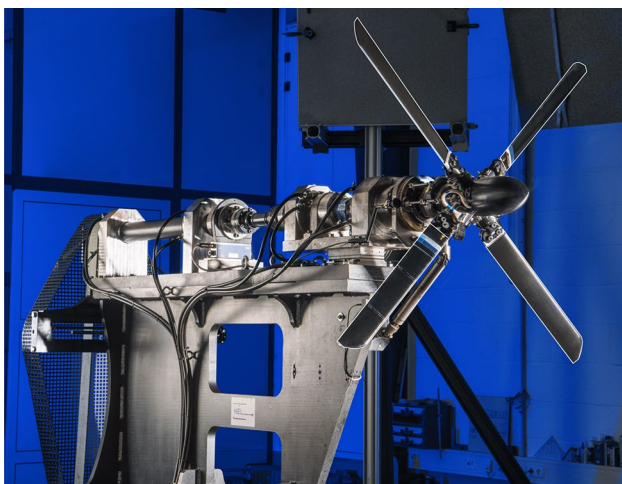


Fig. 1 Four-bladed rotor with parabolic blade tips (see Fig. 2) in the RTG at DLR Göttingen

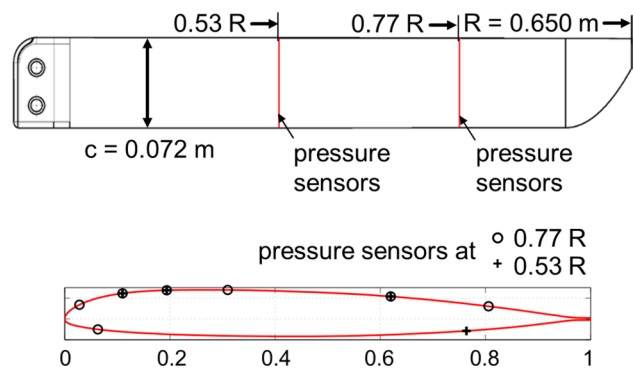


Fig. 2 Top: planview of the rotor blade (Schwermer et al. 2016, not to scale). Bottom: DSA-9A airfoil and location of pressure sensors

at  $r/R = 0.77$  (see Fig. 2, bottom), providing a signal at a bandwidth of 19 kHz.

The rotor head of the RTG featured a swashplate allowing for the adjustment of both collective and cyclic blade pitch angles (Schwermer et al. 2016). The resulting pitch cycle at  $r/R = 0.75$  can be described according to Eq. 1.

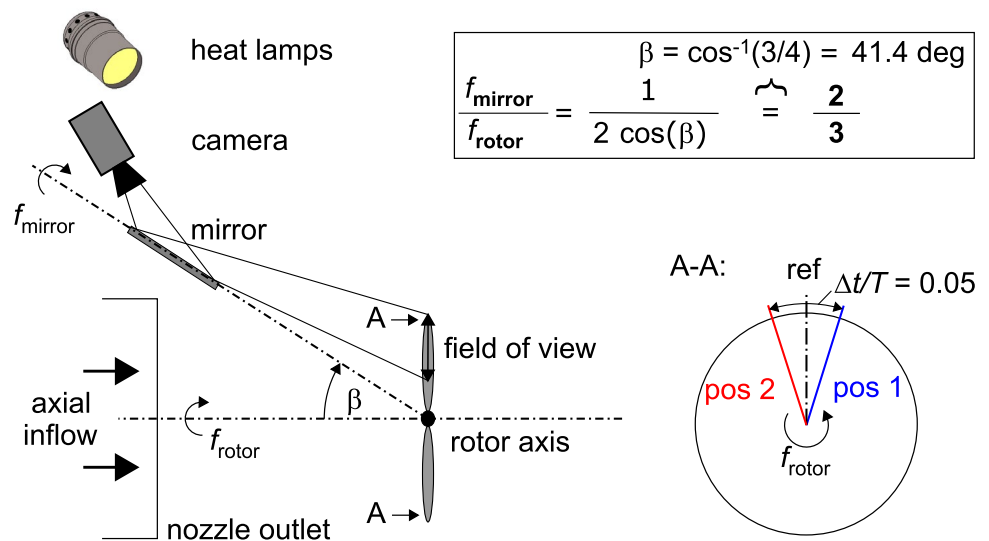
$$\Theta_{75} = \bar{\Theta}_{75} - \hat{\Theta} \cdot \cos(2\pi f_{\text{rotor}} t) \tag{1}$$

In this expression,  $\bar{\Theta}_{75}$  and  $\hat{\Theta}$  are the collective and cyclic pitch settings, and  $f_{\text{rotor}} t = t/T$  is the phase position. With this setting, the pitch cycle started at minimum pitch angle at  $t/T = 0$  and reached the maximum at  $t/T = 0.5$ . While the optical setup was oriented toward a fixed azimuthal blade position, the test rig allowed scanning of the entire pitch cycle within the camera's field of view at that azimuthal position (Schwermer et al. 2019). This was realized by slowly rotating the usually stationary lower part of the swashplate, leading to the blade pitch cycle sweeping through the fixed measurement position.

A schematic sketch of the test setup is shown in Fig. 3. Heat lamps were installed above the nozzle outlet in order to increase the temperature difference between laminar and turbulent flow regions on the blade surface. The resulting radiative heat flux was measured with a power meter and yielded between 400–500 W/m<sup>2</sup> at the rotor disk. Images were acquired with a FLIR Systems™X8500sc SLS high speed infrared camera. The 14 bit camera had a spectral sensitivity in the long wave infrared range of 7.5 – 12 μm and was equipped with a 50 mm, f/2.5 lens located approximately 2 m from the investigated blade. The optical setup was completed by a rotating mirror, which was used to capture a stationary image of the moving blade. This enabled longer exposure times for increased signal strength while avoiding motion-blurred images.

An important feature of the rotating mirror is that it allows to capture two successive rotor blade images within the same rotor revolution at different azimuthal positions,

**Fig. 3** Schematic of rotating mirror setup in off-axis configuration for DIT measurements at the RTG



which correspond to different pitch phases. The rotating mirror was installed in an off-axis configuration as suggested by Raffel and Heineck (2014). It meets the requirement for a ratio of rotation frequencies between rotating mirror to rotor of  $f_{\text{mirror}}/f_{\text{rotor}} = 2/3$ . The ratio enables image acquisition at every third rotor revolution. For unsteady boundary-layer transition measurements (see Sect. 3.2), the setup aims to acquire an image pair (at ‘pos 1’ and ‘pos 2’, see Fig. 3) at all pitch phases and with a phase difference during a single rotor revolution. This allows to capture the instantaneous transition position associated with the pitch angle at the intermediate phase position (marked as ‘ref’ in Fig. 3).

The examined test cases are listed in Table 1. The resulting Mach- and Reynolds numbers as well as the reduced frequency  $k_{75}$  are provided at the radius  $r = 0.75 R$ . The test cases comprise three different pitch amplitudes and two different rotation rates of the rotor, allowing to study the effects of pitch amplitude (test cases I, II and III) and pitch frequency (test cases III and IV) independently. Test case V was selected for comparison to the steady cases with constant collective pitch angle and to numerical simulations, which are described in the next section.

## 2.2 Numerical setup

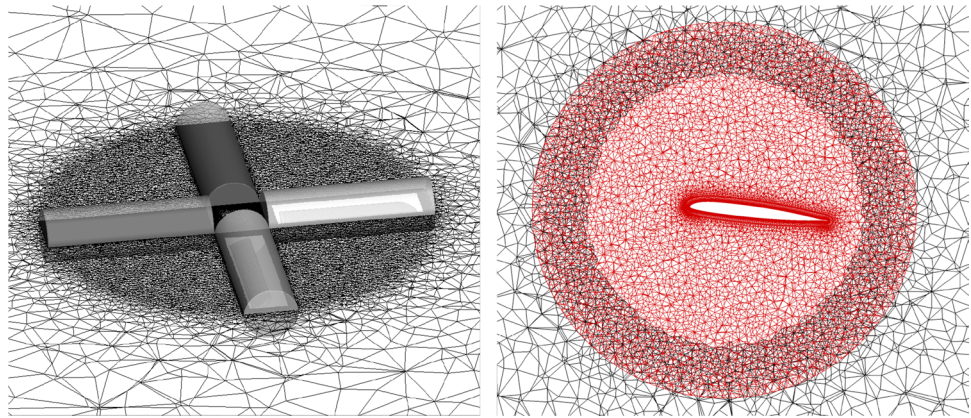
DLR-TAU (see Schwaborn et al. 1994) is an unstructured finite-volume CFD code solving the compressible Navier-Stokes equations. The temporal discretization of the RBT simulations uses an implicit Euler method with a LUSGS linear solver inside a dual time stepping approach. A single blade revolution was discretized into time steps corresponding to  $1^\circ$  azimuth. The setup yielded the same results as computations using a resolution of  $0.1^\circ$  azimuth. The turbulence and transition equations are solved by a flux-difference splitting scheme using Roe averaging with a second-order state extrapolation, and for the diffusive fluxes a second-order central scheme is used. The turbulence is modeled using the  $k-\omega$  SST eddy viscosity model according to Menter (1994).

Both highly resolved and partially scale-resolving transition computations on the NASA PSP rotor, for instance by Coder (2017) and Vieira et al. (2017) have shown the potential of a very detailed transition modeling. Nevertheless, the computational costs of these kind of investigations are still too high for industry-relevant computations. In this study, a very coarse grid and an approximate boundary-layer transition method is used, which is relevant to industry due to the low computational costs. The computations were

**Table 1** Test conditions

Test case	$f_{\text{rotor}}$ , Hz	$\bar{\Theta}_{75}$ , °	$\hat{\Theta}$ , °	$\text{Re}_{75}$	$M_{75}$	$v_\infty$ , m/s	$k_{75}$
I	11.8	10.1	1.6	$1.7 \times 10^5$	0.11	2.2	
II	12.0	10.1	2.9	$1.7 \times 10^5$	0.11	2.2	
III	11.8	9.9	6.2	$1.6 \times 10^5$	0.10	2.2	0.074
IV	23.6	9.6	6.2	$3.3 \times 10^5$	0.21	2.2	
V	23.6	9.0	5.9	$3.2 \times 10^5$	0.21	4.9	
Steady	23.6	2.1–17.1	–	$3.2\text{--}3.3 \times 10^5$	0.21	4.9	–

**Fig. 4** Left: chimera setup for rotor blades; right: grid section at  $r/R = 0.77$



performed using the GCS Supercomputer SuperMUC at the Leibniz Supercomputing Centre. The computations without cyclic lasted  $\approx 10\,000$  CPUh, whereas the cyclic test case V (see Table 1) took  $\approx 20\,000$  CPUh to converge.

The RBT-TAU computations were run on a complete four blade mesh setup, which is depicted in Fig. 4. The hybrid mesh consists of a hexahedral grid around the blade and tetrahedral elements in the farfield. The background farfield mesh is integrated with the blade mesh using the chimera technique. A full cylinder of  $200 R$  height and  $100 R$  radius containing the four blades is used for the RBT computations. Each blade mesh of the RBT case comprises  $1.5 \times 10^6$  points resulting in a total mesh size of  $7.7 \times 10^6$  nodes (see Fig. 4). The first wall spacing was set to keep  $y^+ < 1$ . The blade is discretized with 120 points and 100 points in streamwise and radial direction, respectively. The boundary-layer discretization in wall-normal direction comprises approximately 30 points. The implemented mesh was chosen according to grid convergence requirements as derived by Heister (2018).

The RBT tool is capable of detecting boundary-layer transition due to five different transition mechanisms (Heister 2018), including Tollmien–Schlichting (TS) transition according to Arnal et al. (1984), which is also known as the ‘AHD criterion’. In preceding computations of the same rotor but in a two-bladed configuration, Kaufmann et al. (2019) included all types of transition mechanisms showing that the predictions were only acceptable if TS transition was modeled exclusively. Therefore, only TS transition was modeled in the current study as well.

To evaluate the AHD criterion, section cuts at 48 different radii are defined for both the pressure and the suction side. The computed transition onset positions are then used to control the turbulence model. However, the transitional region is not modeled, i.e., point transition is assumed. To compute the local turbulence level  $Tu$ , using Eq. 2, the flow velocities  $U_{loc}$  and the turbulent kinetic energy  $k$  are extracted from the numerical data at a user-defined distance upstream of the corresponding stagnation point.

$$Tu = 1/U_{loc} \sqrt{2/3 k} \quad (2)$$

To align with the experimental turbulence level, the kinetic energy at the far field boundary has to be set to match the extracted kinetic energy in front of the profile sections. Therefore, the sustaining turbulence concept is locally implemented up to one rotor radius above the rotor in order to reduce the dissipation of the turbulence quantities from the farfield to the rotor (Spalart and Rumsey 2007). For the DLR-TAU transition criteria computations, an iterative approach was applied to match the turbulence level of  $Tu = 0.09\%$  at  $r/R = 0.77$ . The value for  $Tu$  was deduced by Weiss et al. (2018), who conducted transition measurements on the two-bladed DSA-9A rotor in the same facility.

### 3 Data acquisition and processing

#### 3.1 Steady boundary-layer transition measurements

For the steady test cases in Table 1, IR images were exposed for  $57 \mu s$ . As opposed to image acquisition for unsteady transition measurements (see Sect. 3.2 below), only a single image was acquired every third blade revolution as the blade was passing the azimuthal ‘ref’ position (see Fig. 3). Image processing was carried out according to the automated procedure as applied to different steady boundary-layer transition test cases and detailed by Weiss et al. (2017) In the current work, sixteen images were averaged to increase the signal to noise ratio. For each data point, chordwise positions were extracted at various radial positions corresponding to boundary-layer transition  $(x/c)_{tr}$  (at 50% turbulence intermittency), transition onset  $(x/c)_{onset}$ , and transition end  $(x/c)_{end}$ .

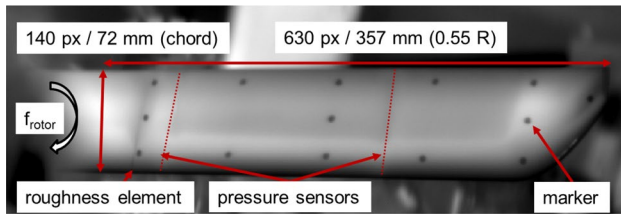


**Fig. 5** Sample image acquired at  $f_{\text{rotor}} = 12.0$  Hz,  $\bar{\Theta}_{75} = 10.1^\circ$  and  $\hat{\Theta} = 2.9^\circ$

### 3.2 Unsteady boundary-layer transition measurements

With every third blade revolution IR images were acquired as the blade was passing the azimuthal positions pos 1 and pos 2 (see Fig. 3) at an exposure time of  $150 \mu\text{s}$ . The azimuthal positions were phase-separated by  $\Delta t/T = \Delta t f_{\text{rotor}} = 0.05$  at all test conditions. The resulting separation times of the image pairs within the same revolution were  $\Delta t = 4.2$  ms and  $2.1$  ms at  $f_{\text{rotor}} = 11.8$  Hz and  $23.6$  Hz, respectively. The separation time was limited by the camera's pixel clock and the selected region of interest, which covers 54% of the rotor radius at a resolution of  $\approx 2$  px/mm (see Fig. 5). At each test condition, the full pitch cycle was recorded by acquiring  $\approx 1000$  image pairs at pos 1 and pos 2, respectively. The resulting phase resolution of the DIT signal is  $\Delta t/T \approx 0.001$ . Since image pairs were acquired with every third blade revolution, data acquisition took approximately 4 min and 2 min for each data point at  $f_{\text{rotor}} = 11.8$  Hz and  $23.6$  Hz, respectively.

The raw image shown in Fig. 5 was acquired for test case II. The displayed gray levels on the blade surface scale with temperature and appear darker in regions of comparatively high heat transfer, for instance close to the leading edge, where the boundary layer is thin, or in the turbulent wake of the roughness element.

Other than for the steady test cases with only collective pitch settings (see Sect. 4.1), the measured intensity gradients in tangential direction cannot be used for instantaneous boundary-layer transition detection on dynamically pitching rotor blades. Previous studies on 2D pitching airfoils have shown that the spatial gradients in the raw images are influenced by the thermal inertia of the model surface (see Raffel and Merz 2014; Wolf et al. 2019; Gardner et al. 2017). Hence, the DIT approach aims to subtract two infrared images acquired at a short time or phase difference within the pitch cycle to capture the transition motion between the two instants at different pitch angles. With this approach, the time-averaged temperature footprint on the model surface is canceled out. In previous DIT studies, the two images were acquired in different pitch cycles at a defined phase difference

because of the limited temporal resolution of the infrared camera (see e.g., Raffel and Merz 2014). Wolf et al. (2019) showed that the resulting large time difference between images can cause global temperature drifts on the model surface, which need to be corrected. In this study, however, the infrared camera captured images during the same rotor revolution at time differences corresponding to acquisition frequencies of up to 476 Hz at the resolution and field of view as described above.

In order to subtract gray levels at the same physical position on the blade, image alignment is necessary. Therefore, round markers (see Figs. 5 and 6) were applied onto the blade surface. Similar as for the steady test cases, marker registration and image alignment were performed with the in-house developed software package *ToPas* (as in Klein et al. 2005). The procedure accounts for rotation and translation within the image plane. Noise was removed by applying a  $3 \times 5$  moving average filter in chordwise and spanwise directions. The aligned images were sorted by phase and the DIT signal  $\Delta I_{\text{DIT}}$  was obtained for each phase according to Eq. 3.

$$\Delta I_{\text{DIT}}(t/T) = [I(t/T)_{\text{pos 1}} - \bar{I}_{\text{pos 1}}] - [I(t/T)_{\text{pos 2}} - \bar{I}_{\text{pos 2}}] \quad (3)$$

Before subtraction of the images at pos 1 and pos 2, tare images according to Eq. 4 are subtracted.

$$\bar{I}_{\text{pos 1|2}} = \frac{1}{N} \sum_{i=1}^{N(\approx 1000)} [I(t/T)_{\text{pos 1|2}}]_i \quad (4)$$

Subtraction of these images accounts for any systematic differences between the two azimuthal positions, for instance due to inhomogeneous heating of the rotor disk area. The phase  $t/T$ , which is associated with the result, corresponds to the mean value of the processed images and the azimuthal position marked as 'ref' in Fig. 3, i.e.,  $t/T = \frac{(t/T)_{\text{pos 1}} + (t/T)_{\text{pos 2}}}{2}$ . The resulting DIT signal has been dewarped to blade coordinates in MATLAB applying a projective image transformation function to calibrated marker coordinates, which have automatically been detected.

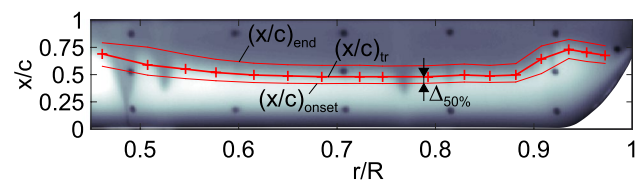


**Fig. 6** Measured transition positions, transition onset and end (in red) over corresponding infrared image at  $\Theta_{75} = 10.0^\circ$ ,  $f_{\text{rotor}} = 23.6$  Hz and  $v_\infty = 4.9$  m/s, rotation is clockwise

## 4 Results

### 4.1 Steady boundary-layer transition

A sample result of the steady transition measurement is displayed in Fig. 6. The positions corresponding to boundary-layer transition  $(x/c)_{tr}$ , transition onset  $(x/c)_{onset}$ , and transition end  $(x/c)_{end}$  are plotted as red lines over the corresponding dewarped IR image. The bright and dark regimes in the image correspond to less and more efficient cooling of the heated blade surface. As argued by Weiss et al. (2017), the points denoted as  $(x/c)_{tr}$  are extracted at the largest intensity gradient of the IR signal from bright to dark and therefore correspond to the point of 50% turbulence intermittency (see Ashill et al. 1996; Stanfield and Betts 1995; Kreplin and Höhler 1992). The points denoted as  $(x/c)_{onset}$  and  $(x/c)_{end}$  are detected in the vicinity of the local maximum curvature of the IR signal upstream and downstream of  $(x/c)_{tr}$  and therefore correspond to the onset and end of the transition region (Ashill et al. 1996; Stanfield and Betts 1995). The visible turbulent wedges are caused by a roughness element, which was applied at  $r/R = 0.49$  as well as triggered by the pressure tap cavities at  $r/R = 0.53$  and  $r/R = 0.77$  (see Fig. 5).

The thrust is evaluated in terms of the blade loading coefficient  $C_T/\sigma = F_{thrust}/[\rho_{\infty}A_{blades}(2\pi f_{rotor}R)^2]$ . Experimental and numerical results for the steady test cases are plotted against the pitch angle in Fig. 7. The bar sizes indicate the linearity error of the piezo-balance being  $\pm 1\%$  of the measured value but at least  $\pm 1$  N. The numerical results exceed the experimental data at lower pitch angles by up to  $\Delta C_T/\sigma = 0.004$  while agreeing within the accuracy limits of the experimental results at the highest pitch angles tested.

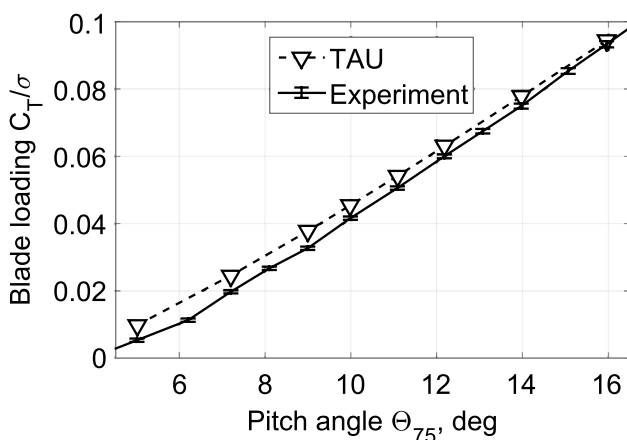


**Fig. 7** Comparison between measured and simulated blade loading for steady test cases at  $f_{rotor} = 23.6$  Hz and  $v_{\infty} = 4.9$  m/s

For the numerical boundary-layer transition solution, the AHD criterion estimates the point of primary instability of TS waves. Therefore, the simulated results represent the transition onset. In order to compare experimental and numerical transition positions corresponding to 50% intermittency (as detected by DIT for the unsteady cases, see Sect. 4.2), the numerical results for  $(x/c)_{onset}$  have to be corrected. The measured difference between the experimental transition position and transition onset,  $\Delta_{50\%} = (x/c)_{tr} - (x/c)_{onset}$ , is plotted as function of  $(x/c)_{onset}$  for all steady test cases at various radial positions (see red '+'-signs in Fig. 6) in Fig. 8. The fitted and dashed curve in red is further used as a correction function. The corresponding values of  $\Delta_{50\%}$  are added to the numerical transition onset to enable comparability to experimental transition positions. The correction function can be interpreted as an intermittency function describing approximately half of the intermittency length along the streamwise coordinate where transition onset is detected. The values reveal a dependency on the streamwise coordinate with a peak at  $(x/c)_{onset} = 0.6$ . It is known that the intermittency length increases as the adverse pressure gradient becomes weaker (Walker and Gostelow 1990). Previous investigations by Weiss et al. (2018) of static transition data on the same rotor blade have shown that the boundary-layer shape factor at transition onset exhibits its minimum in the vicinity of  $x/c = 0.6$ . The lowest shape factor corresponds to the weakest adverse pressure gradient

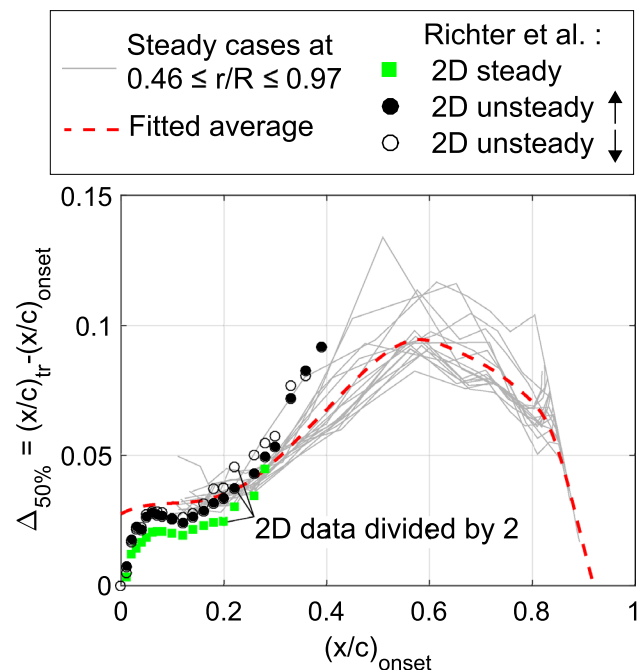


**Fig. 8** Intermittency correction function against transition onset and comparison to 2D airfoil data from Richter et al. (2015)

(Schlichting and Gersten 2017), which therefore explains the distribution of  $\Delta_{50\%}$  in Fig. 8. Richter et al. (2015) measured the full intermittency region on a 2D pitching DSA-9A airfoil suction side with hot-films at  $M = 0.3$  and  $Re = 1.8 \times 10^6$ . Their results are added to Fig. 8. In order to compare only half of the intermittency lengths, their values are divided by two, which yields good agreement with the results from this study. Their unsteady results at pitch angles between  $4^\circ \pm 6^\circ$  and a reduced frequency of 0.060 revealed insignificant differences to the steady data, which justifies the applicability of the correction function to unsteady cases.

Measured and calculated transition results for steady test cases at  $\Theta_{75} = 9^\circ$  and  $14^\circ$  are plotted against the radial coordinate in Fig. 9 (top), while the corresponding numerical sectional lift coefficients  $c_l$  are depicted in Fig. 9 (bottom).

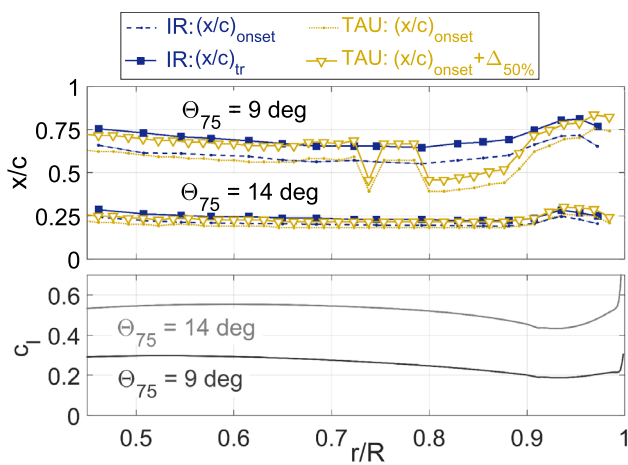


**Fig. 9** Measured (IR) and calculated (TAU) transition data across the blade span (top) and calculated sectional lift coefficients (bottom) for selected steady test cases

The larger lift and the resulting stronger adverse pressure gradients on the blade suction side lead to further upstream transition positions at  $\Theta_{75} = 14^\circ$ . At this pitch angle, measured and calculated values for both  $(x/c)_{tr}$  and  $(x/c)_{onset}$  coincide. For both cases, the experimentally deduced downstream kink of transition positions at  $r/R > 0.9$  is appropriately predicted by the numerical results. The effect can be attributed to the influence of the blade tip vortex, which is also reflected in the spanwise development of the sectional lift coefficient in the graph below. The lift curves comprise a minimum at  $r/R = 0.93$  which is in the spanwise range with the downstream kink of transition positions. At  $\Theta_{75} = 9^\circ$  measured and numerically corrected results for  $(x/c)_{tr}$  show close agreement at  $r/R < 0.72$  and at  $r/R > 0.9$ , which demonstrates that the correction function  $\Delta_{50\%}$  works well. In the spanwise range between  $0.72 < r/R < 0.9$ , the numerical results switch between two levels and deviate by up to  $\Delta(x/c)_{tr} \approx 0.21$  further upstream. It is known from previous steady transition investigations on the same rotor blade by Weiss et al. (2018) that the transition gradient with changing pitch angles is comparatively large in this streamwise range. Hence, the case at  $\Theta_{75} = 9^\circ$  exemplifies that transition positions in this streamwise range are challenging to predict, which was also observed by Kaufmann et al. (2019) for steady cases with the two-bladed rotor configuration at the RTG.

### 4.2 Unsteady boundary-layer transition

Selected DIT results obtained at test case V (see Table 1) during upstroke ( $\uparrow$ ) and downstroke ( $\downarrow$ ) are shown in Fig. 10 (top) and (bottom). The results were obtained at the same instantaneous pitch angle of  $\Theta_{75} = 11.5^\circ$ . During upstroke, boundary-layer transition moves upstream between

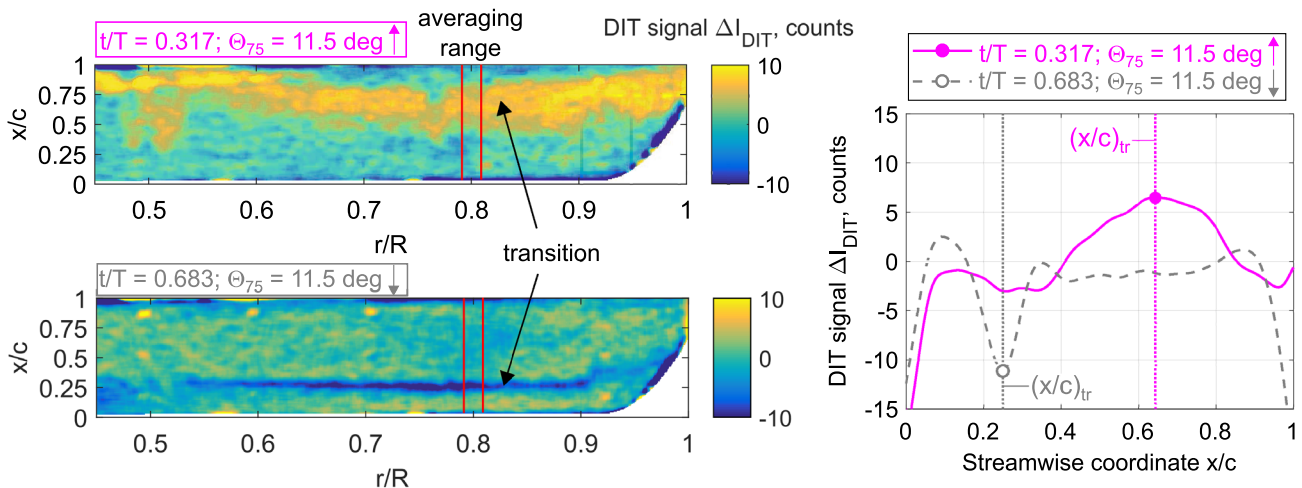


**Fig. 10** DIT results for test case V (see Table 1) at an instantaneous pitch angle of  $\Theta_{75} = 11.5^\circ$   $\uparrow$  (top) and  $\downarrow$  (bottom) with spanwise averaged DIT signals at  $r/R = 0.8$  against streamwise coordinate (right)



the first and the second image. Hence, the spatial extent of more efficiently cooled blade surface is increased and the DIT signal is expected to be positive. The opposite holds true during downstroke. This is confirmed by the results in Fig. 10. At  $t/T = 0.317$ , the DIT signal is positive and appears as yellow band across the blade span. In contrast, the result at  $t/T = 0.683$  on the bottom reveals a prominent band of negative values for  $\Delta I_{\text{DIT}}$  at  $r/R > 0.55$ , which are caused by the downstream movement of boundary-layer transition during downstroke. In Fig. 10 (top), wedge-shaped structures can be distinguished in the DIT signal at  $r/R = 0.49, 0.53$  and  $0.77$ . They correspond to turbulent wedges caused by the roughness element and the pressure tap cavities as was the case for the steady results in Fig. 6.

The transition position is quantified at  $r/R = 0.8$  by analysis of the spanwise averaged signal confined by the red lines in Fig. 10 (top) and (bottom). The averaging interval corresponds to  $\Delta r = 10$  mm, and the corresponding DIT signals are plotted versus the streamwise coordinate  $x/c$  in Fig. 10 (right). The processed DIT data, displayed by the solid and dashed lines for  $t/T = 0.317$  and  $t/T = 0.683$ , were used to find the circled signal peaks. According to Richter et al. (2016) and Gardner et al. (2017), the DIT peak locations are equivalent to the positions corresponding to 50% turbulence intermittency. The DIT peak location is also at the position where the cycle-to-cycle RMS pressure transducer signal peaks (according to the so-called  $\sigma c_p$  method by Gardner and Richter 2015), and therefore considered as the transition position  $(x/c)_{\text{tr}}$  in this work. A comparison of the peak positions in Fig. 10 (right) reveals that transition occurs further upstream by  $\Delta(x/c)_{\text{tr}} \approx 0.4$  at  $t/T = 0.683$  during downstroke compared to  $t/T = 0.317$  during upstroke. Considering that the associated pitch angle is the same for both phases, the observed difference is due to both aerodynamic and temperature-lag related hysteresis effects as previously examined by Gardner et al. (2017) and Wolf et al. (2019) and further discussed below.

For test case V, the DIT signal  $\Delta I_{\text{DIT}}$  was analyzed at  $r/R = 0.8$  for all sampled pitch phases. An automated algorithm detected the peak height  $\Delta I_{\text{DIT}}$  and the corresponding transition position  $(x/c)_{\text{tr}}$ , which are plotted in Fig. 11 (top) and (bottom), respectively. The peak search region was confined to  $\pm 0.4$  chord lengths around the steady transition position at the same pitch angle. The steady case data were linearly interpolated between the measured points, which are displayed by squares in Fig. 11 (bottom). The selected search region includes hysteresis effects and removes invalid outliers. For all other test cases, the search region was confined to  $\pm 0.25$  chord lengths around the transition position detected at the previous phase sample. Peaks were only accepted above a threshold value of  $|\Delta I_{\text{DIT}}| > 5$  counts. The qualitative evolution of

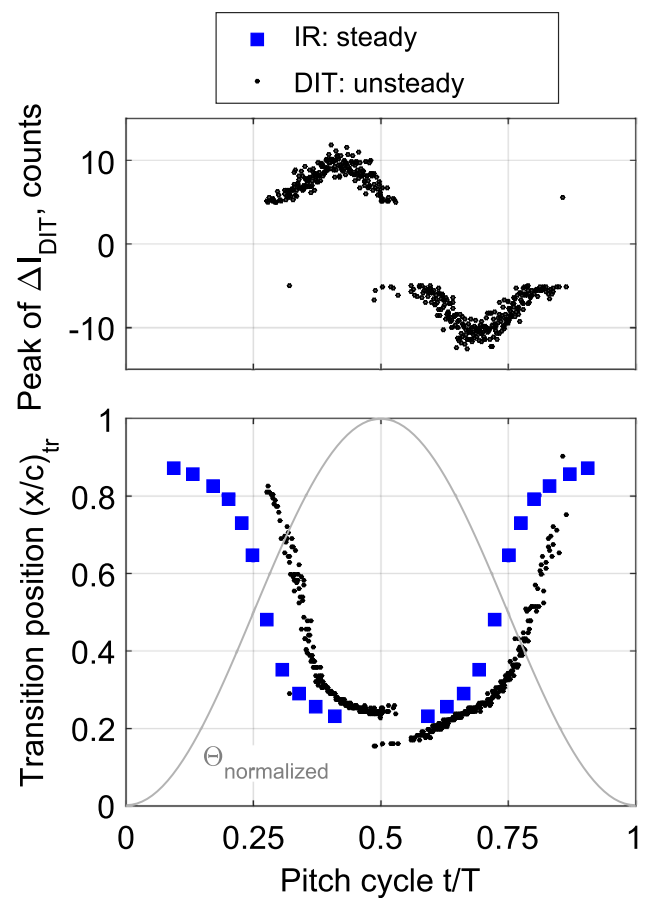


**Fig. 11** DIT results for test case V at  $r/R = 0.8$ : Signal peaks against pitch cycle (top); measured unsteady transition positions against pitch cycle compared to transition positions of steady cases (see Table 1) at associated pitch angles (bottom)

the pitch angle is added in gray to Fig. 11 (bottom) to ease interpretation of the results.

As expected, transition moves upstream at increasing pitch angles and downstream at decreasing pitch angles. The DIT peaks in Fig. 11 (top) are large when the transition motion between the images at pos 1 and pos 2 is fast. Therefore, the peak values have a sinusoidally shaped distribution over the pitch cycle  $t/T$  as also previously observed by Wolf et al. (2019). The measured unsteady transition positions in Fig. 11 (bottom) are spread across a similar chordwise range as compared to the steady IR results, yet exhibit a phase lag of  $\Delta t/T \approx 0.1$ . The underlying hysteresis effects are further discussed below.

Transition detection is difficult at the reverse points of the pitch cycle because DIT relies on changes of the boundary-layer transition position. Similar to the findings in previous DIT studies (Raffel and Merz 2014; Richter et al. 2016; Wolf et al. 2019), the data gap at the downstream transition reverse point close to the pitch minimum is larger than the phase range with spurious data at the pitch maximum reverse

point. At the upstream reversal of  $(x/c)_{tr}$ , the detected peak positions switch back and forth between distinct chordwise positions. Richter et al. (2016) and Wolf et al. (2019) found that this behavior is due to the coexistence of the positive and negative signal peaks, which are associated with the upstream and downstream movement of transition (see Fig. 11, bottom).

### 4.2.1 Pitch rate effects on unsteady boundary-layer transition

The effect of pitch rate on unsteady boundary-layer transition is studied with respect to the detectability by means of DIT and the measured transition movement over the pitch cycle. According to the definition of the pitch cycle in Eq. 1, the corresponding pitch rate yields

$$\frac{d\Theta}{dt} = 2\pi f_{rotor} \hat{\Theta} \cdot \sin(2\pi f_{rotor} t). \tag{5}$$

The pitch rate was altered by an independent variation of the pitch amplitude  $\hat{\Theta}$  and the rotation frequency  $f_{rotor}$ . The pitch amplitudes varied between  $\hat{\Theta} = 1.6, 2.9$  and  $6.2^\circ$  at constant collective pitch and pitch frequency (test cases I, II and III in Table 1). The effect of pitch frequency is investigated by changing the rotation rate of the rotor from  $f_{rotor} = 11.8$  Hz to  $f_{rotor} = 23.6$  Hz, leaving collective and cyclic pitch unaltered (test cases III and IV in Table 1).

**Detectability** The DIT signal strength is quantified for each test case by calculating the averaged absolute value of the DIT signal peaks around  $\Delta(t/T) = \pm 0.025$  of the maximum and minimum values of the DIT peaks over the pitch cycle (see e.g., Fig. 11, top). The peak noise, or scatter, is quantified by the averaged standard deviation of the peak values within the same phase ranges, which were considered

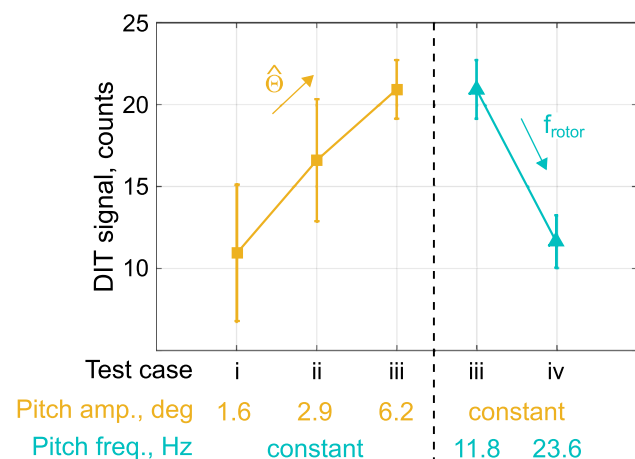


Fig. 12 Maximum averaged absolute value of DIT signal peak and associated scatter for test cases I–IV

to compute the signal strength. The signal strength and the associated scatter are plotted for the test cases used to study the effect of pitch amplitude and pitch frequency in Fig. 12.

The maximum signal peak increases and the scatter decreases with increasing pitch amplitude, which consequently favors the detectability of boundary-layer transition by means of DIT. The increased peak-to-noise ratio at higher pitch amplitudes is due to the larger displacement of the boundary-layer transition position between the time instants of the two associated images. This was demonstrated by Wolf et al. (2019), who applied the DIT method to steady infrared transition data, which has been obtained at different angles of attack on a two-dimensional DSA-9A airfoil (see Fig. 8 in Wolf et al. 2019). However, Wolf et al. (2019) also showed that, if the transition displacement is too large, for instance due to an excessive phase separation between images  $\Delta t/T$ , the detectability is debased due to the existence of a double peak in the signal.

The results in Fig. 12 for test cases III and IV indicate that the maximum signal peak decreases as the pitch frequency is increased, whereas the scatter level remains similar. For all cases, the phase separation between DIT image pairs was kept constant at  $\Delta t f_{rotor} = 0.05$ . Therefore, the time difference between two images is doubled as the frequency is halved. Hence, at  $f_{rotor} = 11.8$  Hz the model surface has twice the time to react to the different surface temperature between images. The transition shift is the same for both pitch frequencies as it depends on the difference in pitch angles  $\Delta\Theta = (d\Theta/dt) \cdot \Delta t$ . The change of pitch angles is also unaltered for the both cases because the

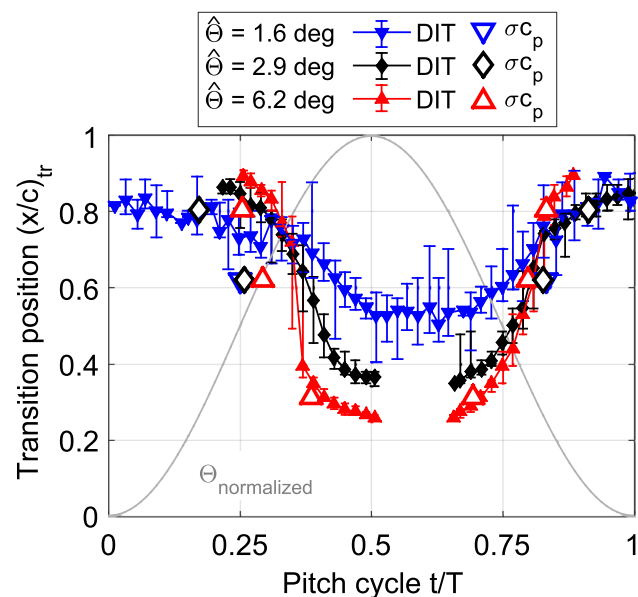


Fig. 13 Pitch amplitude effect on transition positions versus pitch cycle for test cases I, II and III (see Table 1); DIT data extracted at  $r/R = 0.74$ ,  $\sigma_{c_p}$  data at  $r/R = 0.77$

phase separation  $\Delta t_{f_{\text{rotor}}}$  between images is constant, i.e.,  $\Delta\Theta = 2\pi\Delta t_{f_{\text{rotor}}} \cdot \sin(2\pi f_{\text{rotor}}t)$ , see Eq. 5.

**Transition positions** The measured boundary-layer transition positions for the pitch amplitude study are plotted against the pitch cycle in Fig. 13. For reasons of clarity, the data in Fig. 13 and the following figures have been reduced. All data samples were binned to 50 windows throughout the pitch cycle and each bin was median filtered to smooth out existing scatter. The bars confine the minimum and maximum of the data considered for each bin, respectively. Before binning, obvious invalid outliers were removed, for instance in phase ranges close to the pitch minimum or at streamwise positions in the vicinity of the leading and trailing edges.

In Fig. 13, DIT data is extracted at  $r/R = 0.74$ , which is in the vicinity of the pressure transducers at  $r/R = 0.77$  but outside the turbulent wedge emanating from the sensor cavities. The streamwise range of occurring boundary-layer transition is extended to both directions as the pitch amplitude is increased, leading to an intersection of the scatter plots at  $t/T \approx 0.35$  and  $t/T \approx 0.81$ . These phases are in the vicinity of the phases corresponding to the respective mean pitch angle, i.e.,  $t/T = 0.25$  and  $t/T = 0.75$ . The same effect was observed by Richter et al. (2014), who studied the pitch amplitude effect on unsteady boundary-layer transition on a two-dimensional (2D) EDI-M109 airfoil. They showed that the intersection points correspond to phases with comparable sectional lift coefficient.

To compare with DIT results, the  $\sigma_{c_p}$  method was applied according to Gardner and Richter (2015). The detected phases corresponding to boundary-layer transition at the respective sensor positions are marked by open symbols in Fig. 13. The  $\sigma_{c_p}$  results compare well during downstroke and comprise a maximum difference of  $\Delta(x/c)_{\text{tr}} \approx 0.25$  during upstroke. The upstream shift compared to the DIT results at  $t/T < 0.5$  can be attributed to premature boundary-layer transition at the pressure tap cavities as observed in Fig. 10 (top) at  $r/R = 0.77$ .

The measured transition positions for the pitch frequency study are plotted against the pitch cycle in Fig. 14. The qualitative evolution of the transition positions is similar to the results discussed in Fig. 13. In general, the unsteady transition results are consistently further upstream at the higher pitch frequency of  $f_{\text{rotor}} = 23.6$  Hz. Since the axial inflow remains unchanged in both cases, the inflow angle to the rotor blades increases at higher rotation rates. The resulting larger effective angle of attack causes a higher blade loading of  $C_T/\sigma = 0.053$  at  $f_{\text{rotor}} = 23.6$  Hz compared to  $C_T/\sigma = 0.038$  at  $f_{\text{rotor}} = 11.8$  Hz, which, in turn, results in boundary-layer transition positions further upstream. The higher Reynolds number at  $f_{\text{rotor}} = 23.6$  Hz also causes boundary-layer transition to occur upstream. Hence, the results in Fig. 14 include the superposed

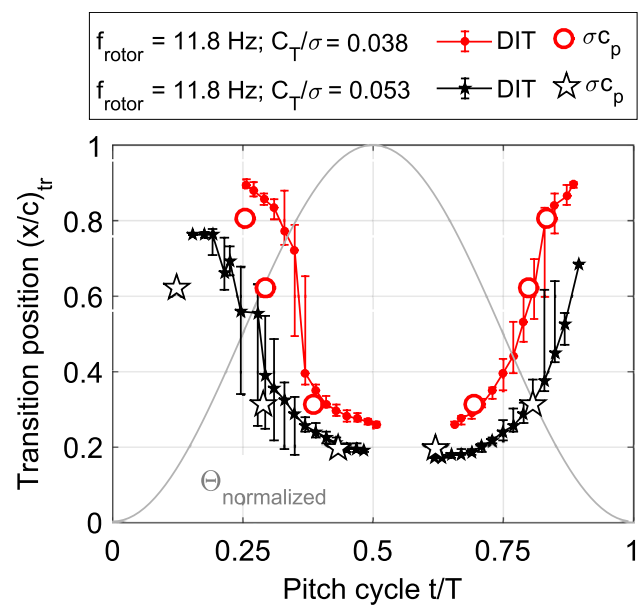


**Fig. 14** Pitch frequency effect on transition positions versus pitch cycle for test cases III and IV (see Table 1); DIT data extracted at  $r/R = 0.79$ ,  $\sigma_{c_p}$  data at  $r/R = 0.77$

effects of both Reynolds number and blade loading. As for the cases presented in Fig. 13, the  $\sigma_{c_p}$  results indicate boundary-layer transition further upstream during upstroke and good agreement to DIT results during downstroke. At  $(x/c)_{\text{tr}} = 0.62$  in Fig. 14, only a single peak in the  $\sigma_{c_p}$  measuring signal could be identified. It occurs close to the reversal of the transition motion and was attributed to the upstroke motion.

**Transition hysteresis** The effects of pitch amplitude and frequency on the transition hysteresis become more apparent in Fig. 15, where the measured transition positions are plotted as function of the instantaneous pitch angle for the test cases presented in Figs. 13 and 14, respectively.

The results in Fig. 15 (top) indicate that the hysteresis, i.e., the difference in pitch angle at equal transition position, increases with pitch amplitude. The finding confirms the results of the pitch amplitude study by Richter et al. (2014) and extends the applicability to rotor conditions. Moreover, a smaller hysteresis is measured using  $\sigma_{c_p}$  compared to DIT. This holds true for the transition positions of the test cases used in order to study the effect of pitch frequency in Fig. 15 (bottom), as well.

Richter et al. (2015, 2016) measured the isolated effect of pitch frequency on the transition hysteresis on a pitching 2D DSA-9A airfoil at  $M = 0.30$  and  $Re = 1.8 \times 10^6$ . The hot-film results by Richter et al. (2015) were compared to the findings using DIT and  $\sigma_{c_p}$  in Richter et al. (2016). Wolf et al. (2019) studied the effect of both pitch amplitude and frequency on the transition hysteresis. They used the same 2D DSA-9A airfoil model as Richter et al. (2015, 2016). One

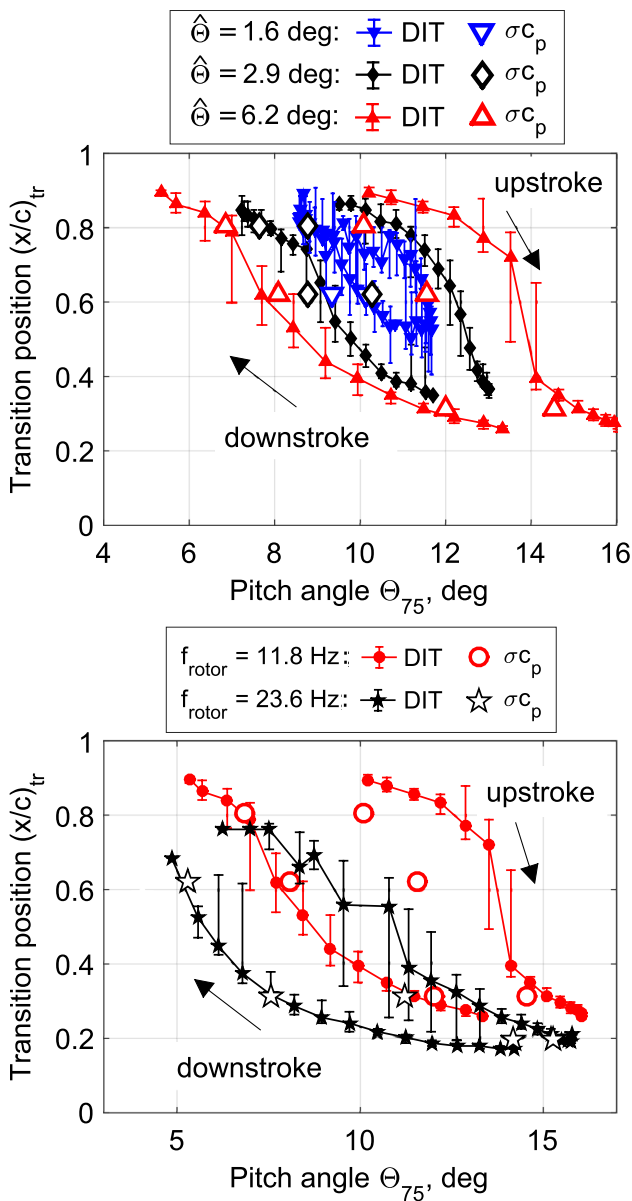


Fig. 15 Unsteady transition positions versus pitch angle for different pitch amplitudes (top) and different pitch frequencies (bottom)

of their findings showed that the hystereses were obtained by  $\sigma_{c_p}$  and DIT scale with the respective pitch rates (see Eq. 5). The hystereses measured by Richter et al. (2016) and Wolf et al. (2019) are plotted in Fig. 16 (top) as functions of the pitch rate with filled symbols representing DIT and open symbols standing for  $\sigma_{c_p}$ .

The pitch rate associated with each data point is calculated as the mean value between the two phases when transition passes the streamwise position of the respective pressure transducers. Richter et al. (2016) extracted the data at  $(x/c)_{tr} = 0.22$  and at  $(x/c)_{tr} = 0.23$  for DIT and  $\sigma_{c_p}$ , respectively. The data from Wolf et al. (2019) are acquired at

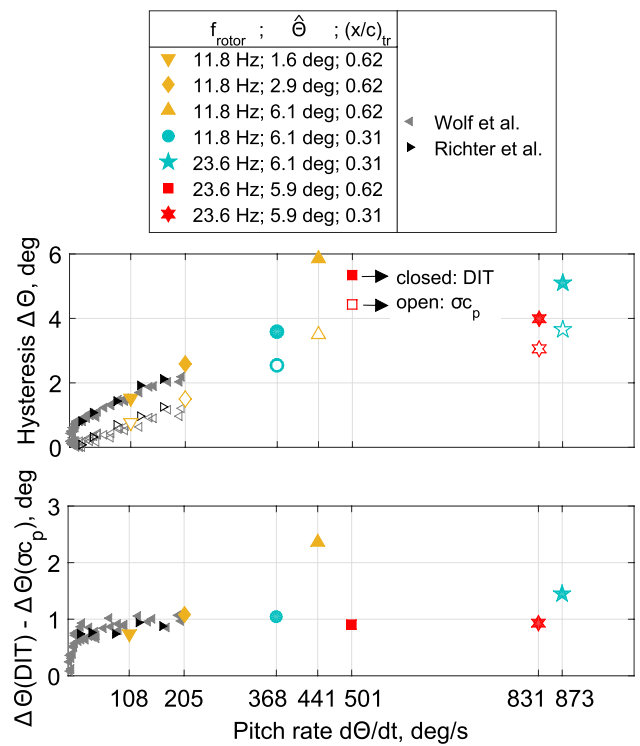


Fig. 16 Hysteresis obtained with DIT and  $\sigma_{c_p}$  (top) and temperature-lag related hysteresis (bottom) against pitch rate compared to results from Wolf et al. (2019) and Richter et al. (2016)

$(x/c)_{tr} = 0.31$ . The graph is complemented by the hystereses measured in this study at  $(x/c)_{tr} = 0.62$  and at  $(x/c)_{tr} = 0.31$ . At these streamwise positions, data for both DIT and  $\sigma_{c_p}$  could be extracted for the test cases used to study the effect of pitch amplitude (in orange), of pitch frequency (in blue), and for test case V (in red). The observed trends by Richter et al. (2016) and Wolf et al. (2019), i.e., the increasing hysteresis at increasing pitch rates for results obtained by both DIT and  $\sigma_{c_p}$ , are confirmed by the data presented in this paper. Additionally, the results from this work extend the range of existing pitch rate data from  $d\Theta/dt < 200^\circ/s$  up to  $d\Theta/dt = 873^\circ/s$ , while providing the first transition hysteresis data set obtained by DIT on rotating blades so far.

The hysteresis obtained with DIT includes an additional temperature-lag related hysteresis due to the model surface time response to the changing temperature footprint as result of the boundary-layer transition displacement (Richter et al. 2016; Wolf et al. 2019; Gardner et al. 2017). Assuming that the hysteresis values obtained by  $\sigma_{c_p}$  display the aerodynamic hysteresis only, the differences between the results from DIT and  $\sigma_{c_p}$  [ $\Delta\Theta(DIT) - \Delta\Theta(\sigma_{c_p})$ ], express the temperature-lag related measurement hysteresis of DIT (see Wolf et al. 2019). The measurement hysteresis is plotted as a function of

pitch rate in Fig. 16 (bottom). The results from Wolf et al. (2019) indicate a convergence of  $\Delta\Theta(DIT) - \Delta\Theta(\sigma_{c_p})$  to  $\approx 1^\circ$ , which includes the results from Richter et al. (2016). The prescribed trend is confirmed by all data points from the present study, except for the outlier at  $d\Theta/dt = 441^\circ/s$ . Wolf et al. (2019) showed that the measurement hysteresis is minimized when limiting the phase separation between the acquired images for DIT to  $\Delta t_f < 0.01$ , which applies to their data in Fig. 16. The results in this study are acquired at phase differences of  $\Delta t_{f_{rotor}} = 0.05$  and the data points from Richter et al. (2016) are obtained at phase differences between  $0.006 < \Delta t_f < 0.046$  with greater values at higher pitch rates. However, the data in Fig. 16 (bottom) at  $d\Theta/dt < 205^\circ/s$  do not indicate any influence by the different phase deltas.

### 4.2.2 Transition map

Test case V (see Table 1) was selected for further analysis of transition positions across the blade span over the entire pitch cycle. The experimental and numerical results are shown in Fig. 17 (left) and (right), respectively. Both ‘transition maps’ comprise the same contour levels, and the data are plotted in polar coordinates with the pitch cycle and the corresponding pitch angles in counter-clockwise direction and with the normalized blade radius in radial direction. Overall, the results reveal remarkable agreement.

The experimental data were analyzed at seventeen radial positions between  $0.26 \leq r/R \leq 0.97$ . For each radius, the detected transition positions were cleared from outliers and valid data were median filtered to 50 bins within the pitch cycle as described above. The resulting contour plot in Fig. 17 (left) is derived from the measured boundary-layer transition positions  $(x/c)_{tr}$  as well as from 2D linearly

interpolated data at grid points corresponding to the nearest phase position with available data and the seventeen evaluated radial sections. The phase shift of maximal upstream and downstream transition positions due to hysteresis effects with respect to the vertical axis in the plot is clearly distinguishable. The data displayed in the bottom left and top right quadrant of the graph at  $0.25 < t/T < 0.5$  and  $0.75 < t/T < 1$  reveal the gradual upstream and downstream movement of transition during upstroke and downstroke, respectively. The three-dimensional distribution of  $(x/c)_{tr}$  along the blade span can be deduced by the curved isolines between contour levels. At phase instants between  $0.3 < t/T < 0.45$ , boundary-layer transition occurs further upstream at more outboard radii, whereas between  $0.75 < t/T < 0.87$  transition is shifted downstream at higher radii. In the same phase domains, the measured transition positions reveal a noticeable downstream shift at the most outboard radii of  $r/R > 0.85$ .

The numerical results in Fig. 17 (right) have been corrected by the measured delta between transition onset and the point of 50% intermittency using the correction function  $\Delta_{50\%}$  from Fig. 8. The numerical data were extracted at 48 line-in-flight cuts at each time step, which corresponds to  $\Delta(t/T) = 1/360$ . The two data sets show good quantitative and qualitative agreement, especially with respect to the curvature of contour isolines at  $0.25 < t/T < 0.5$  and  $0.75 < t/T < 1$ . As suggested by the measurement results at  $r/R > 0.85$ , the numerical results in these phase domains confirm the downstream shift of boundary-layer transition toward the blade tip, as found in the steady test cases in Sect. 4.1. In between  $0.3 < t/T < 0.4$ , a relative upstream shift of the experimental transition positions can be distinguished in the vicinity of  $r/R = 0.5$ , which is not visible in the numeric result. In this region, the

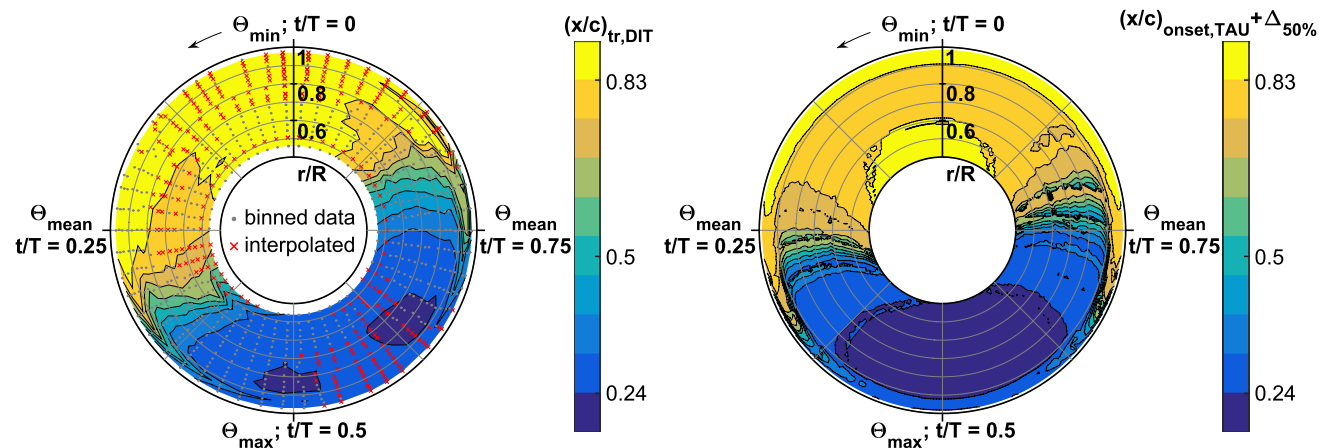


**Fig. 17** Unsteady boundary-layer transition map at  $f_{rotor} = 23.6$  Hz,  $\Theta_{75} = 9.0^\circ$  and  $\Theta = 5.9^\circ$  as measured with DIT (left) and calculated in TAU (right); measured and calculated data in this figure are

available online at [http://www.as.dlr.de/files/supplementary/Unsteady\\_transition\\_data\\_Weiss\\_et\\_al/](http://www.as.dlr.de/files/supplementary/Unsteady_transition_data_Weiss_et_al/)

measurement results were sampled in between the roughness element at  $r/R = 0.49$  and the pressure transducer cavities at  $r/R = 0.53$ , yet the detected positions remain to be influenced by the turbulent wedges at these radii (see Fig. 10, top).

The numerically predicted upstream and downstream motion of boundary-layer transition is faster than the measured data suggests. This is indicated by the closer spacing of contour isolines for the numerical solution as compared to the experimental results at the phases during upstroke and downstroke when  $\Theta_{\text{mean}}$  is passed. Moreover, the numerical results during upstroke at  $t/T \approx 0.3$  and during downstroke at  $t/T \approx 0.8$  indicate a discontinuous transition movement. Experimental and numerical results of test case V, displayed in Fig. 17, are available online ([http://www.as.dlr.de/files/supplementary/Unsteady\\_transition\\_data\\_Weiss\\_et\\_al/](http://www.as.dlr.de/files/supplementary/Unsteady_transition_data_Weiss_et_al/)) together with the rotor blade geometry and can be used by others to validate their own transition prediction capabilities, for instance.

The data shown in Fig. 17 are extracted at  $r/R = 0.75$  and plotted as function of the pitch angle together with the measured results using the  $\sigma_{c_p}$  method in Fig. 18.

The corrected numerical transition positions and the measured DIT results cover the same streamwise range. The TAU and DIT solutions agree especially during downstroke. The closer spacing of contour level lines observed in Fig. 17 is reflected by the larger gradient of the curves for the TAU solution. In Fig. 18, the discontinuities in the numerical results appear as spikes and occur especially in regions, where the adverse pressure gradient is moderate between

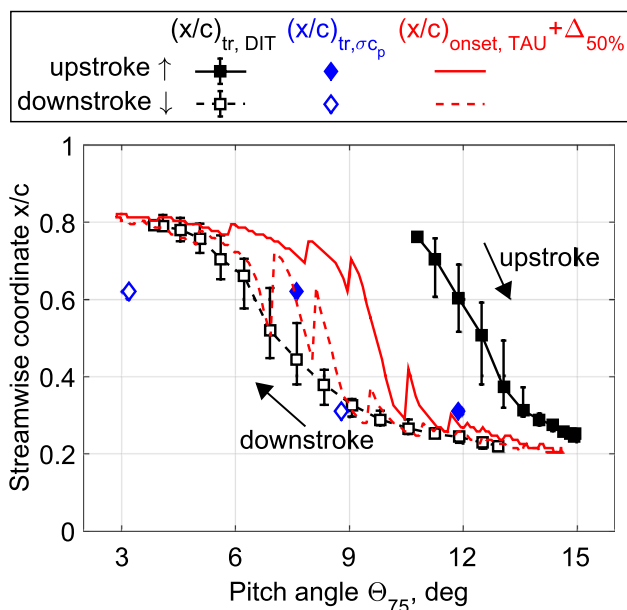


Fig. 18 Measured (DIT,  $\sigma_{c_p}$ ) and calculated (TAU) transition results at  $r/R = 0.75$  for test case V

$0.3 \leq x/c \leq 0.7$  (see Weiss et al. 2018). In this region, also the experimental DIT data exhibits larger scatter as expressed by the black bars. The increased scatter in the numerical results is due to the sensitivity of the transition prediction to small perturbations in the pressure distribution, which is used for the calculation of integral boundary-layer quantities (see also Heister 2018).

Both, numerical and experimental results yield transition positions further downstream during upstroke as compared to during downstroke. Still, there is a noticeable difference of the transition hysteresis magnitude between numerical and experimental results. Although the hysteresis of the numerical solution is hard to quantify due to the spikes in the data, it can be distinguished that the hysteresis of the calculated results is smaller than the hysteresis indicated by the  $\sigma_{c_p}$  results, which are assumed to represent the true aerodynamic hysteresis. Richter et al. (2015) measured the transition hysteresis using hot-films on a 2D pitching DSA-9A airfoil. They showed that the transition hysteresis (in terms of pitch-angle difference between upstroke and downstroke for the same transition position) exceeds the hysteresis in lift. They also measured identical transition positions for different pressure distributions during upstroke and downstroke and argued that the unsteady transition behavior is not just caused by the hysteresis in lift but additionally includes a viscous history which is not included in the pressure distribution. Their finding was supported by the study of Gardner et al. (2019a) who measured different transition positions at similar lift coefficients using the  $\sigma_{c_p}$  method on a 2D pitching DSA-9A airfoil. The numerical transition positions in this study are solely based on the instantaneous pressure distributions. Neither the instantaneous boundary-layer velocity profiles

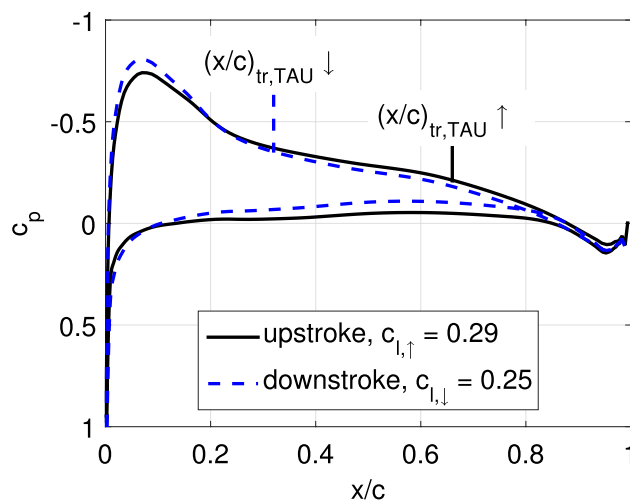


Fig. 19 Numerical pressure distribution at  $\Theta_{75} = 9.0^\circ$  during upstroke and downstroke with corrected transition positions and sectional lift coefficient at  $r/R = 0.75$  for test case V

nor the propagation velocity of Tollmien-Schlichting waves are taken into account in the current version of the RBT tool, causing the numerical hysteresis to be smaller than the measured hysteresis using the  $\sigma_{c_p}$  method.

Further insights into the numerical transition and lift hystereses are provided in Fig. 19, where the instantaneous pressure distributions are provided at the mean pitch angle of test case V, i.e., at  $\Theta_{75} = 9.0^\circ$ , during upstroke and downstroke, respectively. The corresponding transition positions and sectional lift coefficients are also indicated. Although less lift is produced during the downstroke case, the adverse pressure gradients just downstream of the suction peak are stronger during downstroke as compared to during upstroke, which causes transition to occur further upstream.

## 5 Conclusion

This work presents the first systematic study of measured unsteady boundary-layer transition on the suction side of a subscale helicopter rotor blade equipped with a DSA-9A airfoil. The analysis of measured results is complemented by a comparison to numerical computations using the semi-empirical AHD criterion to model boundary-layer transition due to Tollmien-Schlichting instabilities. The main findings are summarized as follows:

- Unsteady boundary-layer transition positions have successfully been measured, showing reasonable comparison to measurement results for steady test cases with collective pitch angles only and deviations due to hysteresis effects.
- The detectability of transition positions by DIT, in terms of signal peak-to-noise ratio, increases with increasing pitch amplitude and decreases with increasing pitch frequency at constant phase differences between images.
- The independent variations of pitch amplitude and pitch frequency reveal plausible trends with respect to the measured transition movement and the related hysteresis.
- Transition positions measured using the  $\sigma_{c_p}$  method show reasonable agreement to DIT results. Deviations are due to premature boundary-layer transition triggered at the pressure tap cavities and due to the temperature-lag related measurement hysteresis in DIT.
- Hysteresis effects, both aerodynamic and for DIT also temperature-lag related, scale with pitch rate. Previous findings obtained on 2D pitching airfoils are confirmed and extended to rotor conditions for pitch rates of up to  $d\Theta/dt = 873^\circ/s$ .

- Transition maps of unsteady experimental and numerical results reveal the three-dimensional distribution of the transition positions along the blade span as function of the pitch cycle. The results obtained by numeric modeling of unsteady boundary-layer transition yield noticeable agreement with experimental results.

**Acknowledgements** Open Access funding provided by Projekt DEAL. The authors would like to thank Anthony D. Gardner and Markus Krebs (DLR Göttingen) for their fruitful advice and the assistance during experiments. Moreover, the Gauss Centre for Supercomputing e.V. ([www.gauss-centre.eu](http://www.gauss-centre.eu)) is gratefully acknowledged for funding this project by providing computing time using the GCS SuperMUC at the Leibniz Supercomputing Centre (LRZ, [www.lrz.de](http://www.lrz.de)).

**Open Access** This article is licensed under a Creative Commons Attribution 4.0 International License, which permits use, sharing, adaptation, distribution and reproduction in any medium or format, as long as you give appropriate credit to the original author(s) and the source, provide a link to the Creative Commons licence, and indicate if changes were made. The images or other third party material in this article are included in the article's Creative Commons licence, unless indicated otherwise in a credit line to the material. If material is not included in the article's Creative Commons licence and your intended use is not permitted by statutory regulation or exceeds the permitted use, you will need to obtain permission directly from the copyright holder. To view a copy of this licence, visit <http://creativecommons.org/licenses/by/4.0/>.

## References

- Arnal D, Habiballah M, Coustols E (1984) Laminar instability theory and transition criteria in two and three-dimensional flow. *La Recherche Aéronautique* (English Edn) 2:45–63
- Ashill PR, Betts CJ, Gaudet IM (1996) A wind tunnel study of transition flows on a swept panel wing at high subsonic speeds. In: CEAS 2nd European forum on laminar flow technology, Bordeaux, France
- Carnes JA, Coder JG (2019) Computational assessment of laminar-turbulent transition for a rotor in forward-flight conditions. In: VFS 75th annual forum & technology display, Philadelphia, PA, USA
- Coder JG (2017) OVERFLOW rotor hover simulations using advanced turbulence and transition modeling. In: 55th AIAA aerospace sciences meeting, Grapevine, TX, USA, <https://doi.org/10.2514/6.2017-1432>
- Gardner AD, Richter K (2015) Boundary layer transition determination for periodic and static flows using phase-averaged pressure data. *Exp Fluids* 56(6):119–131. <https://doi.org/10.1007/s00348-015-1992-9>
- Gardner AD, Eder C, Wolf CC, Raffel M (2017) Analysis of differential infrared thermography for boundary layer transition detection. *Exp Fluids* 58(9):122–135. <https://doi.org/10.1007/s00348-017-2405-z>
- Gardner AD, Merz CB, Wolf CC (2019a) Effect of sweep on a pitching finite wing. *J Am Helicopter Soc* 64(032007):1–13. <https://doi.org/10.4050/JAHS.64.032007>
- Gardner AD, Wolf CC, Heineck JT, Barnett M, Raffel M (2019b) Helicopter rotor boundary layer transition measurement in

- forward flight using an infrared camera. In: VFS 75th annual forum & technology display, Philadelphia, PA, USA
- Heister CC (2012) Semi-/empirical transition prediction and application to an isolated rotor in hover. *Int J Eng Syst Model Simul.* <https://doi.org/10.1504/IJESMS.2012.044845>
- Heister CC (2018) A method for approximate prediction of laminar-turbulent transition on helicopter rotors. *J Am Helicopter Soc* 63(3):1–14. <https://doi.org/10.4050/JAHS.63.032008>
- Kaufmann K, Ströer P, Richez F, Lienard C, Gardarein P, Krimmelbein N, Gardner AD (2019) Validation of boundary-layer-transition computations for a rotor with axial inflow. In: VFS 75th annual forum & technology display, Philadelphia, PA, USA
- Klein C, Engler RH, Henne U, Sachs WE (2005) Application of pressure-sensitive paint for determination of the pressure field and calculation of the forces and moments of models in a wind tunnel. *Exp Fluids* 39(2):475–483. <https://doi.org/10.1007/s00348-005-1010-8>
- Kreplin HP, Höhler G (1992) Application of the surface hot film technique for laminar flow investigations. In: 1st European forum on laminar flow technology, Hamburg, Germany
- Lorber PF, Carta FO (1992) Unsteady transition measurements on a pitching three-dimensional wing. In: 5th symposium on numerical and physical aspects of aerodynamic flows, Long Beach, CA, USA
- Menter FR (1994) Two-equation eddy-viscosity transport turbulence model for engineering applications. *AIAA J* 32(8):2066–2072. <https://doi.org/10.2514/3.12149>
- Min BY, Reimann CA, Wake B, Jee SK, Baeder JD (2018) Hovering rotor simulation using OVERFLOW with improved turbulence model. In: 56th AIAA aerospace sciences meeting, Kissimmee, FL, USA. <https://doi.org/10.2514/6.2018-1779>
- Overmeyer AD, Martin PB (2017) Measured boundary layer transition and rotor hover performance at model scale. In: 55th AIAA aerospace sciences meeting, Grapevine, TX, USA. <https://doi.org/10.2514/6.2017-1872>
- Overmeyer AD, Heineck JT, Wolf CC (2018) Unsteady boundary layer transition measurements on a rotor in forward flight. In: AHS international 74th annual forum & technology display, Phoenix, AZ, USA
- Parwani A, Coder JG (2018) Effect of laminar-turbulent transition modeling on PSP rotor hover predictions. In: 56th AIAA aerospace sciences meeting, Kissimmee, FL, USA. <https://doi.org/10.2514/6.2018-0308>
- Raffel M, Heineck JT (2014) Mirror-based image derotation for aerodynamic rotor measurements. *AIAA J* 52(6):1337–1341. <https://doi.org/10.2514/1.J052836>
- Raffel M, Merz CB (2014) Differential infrared thermography for unsteady boundary-layer transition measurements. *AIAA J* 52(9):2090–2093. <https://doi.org/10.2514/1.J053235>
- Raffel M, De Gregorio F, de Groot K, Schneider O, Sheng W, Gibertini G, Seraudie A (2011) On the generation of a helicopter aerodynamic database. *Aeronaut J* 115(1164):103–112. <https://doi.org/10.1017/S0001924000005492>
- Richez F, Nazarians A, Lienard C (2017) Assessment of laminar-turbulent transition modeling methods for the prediction of helicopter rotor performance. In: 43rd European rotorcraft Forum, Milan, Italy
- Richter K, Koch S, Gardner AD, Mai H, Klein A, Rohardt CH (2014) Experimental investigation of unsteady transition on a pitching rotor blade airfoil. *J Am Helicopter Soc* 59(1):1–12. <https://doi.org/10.4050/JAHS.59.012001>
- Richter K, Koch S, Goertler A, Lütke B, Wolf CC, Benkel A (2015) Unsteady boundary layer transition on the DSA-9A rotor blade airfoil. In: 41st European rotorcraft forum, Munich, Germany
- Richter K, Wolf CC, Gardner AD, Merz CB (2016) Detection of unsteady boundary layer transition using three experimental methods. In: 54th AIAA aerospace sciences meeting, San Diego, CA, USA. <https://doi.org/10.2514/6.2016-1072>
- Schlichting H, Gersten K (2017) Boundary-layer theory, 9th edn. Springer, Berlin. <https://doi.org/10.1007/978-3-662-52919-5>
- Schwamborn D, Gerhold T, Heinrich R (1994) The DLR TAU-code: recent applications in research and industry. *AIAA J* 32(8):2066–2072. <https://doi.org/10.2514/3.12149>
- Schwermer T, Richter K, Raffel M (2016) Development of a Rotor Test Facility for the Investigation of Dynamic Stall. In: Dillmann A, Heller G, Krämer E, Wagner C, Breitsamter C (eds) New results in numerical and experimental fluid mechanics X, vol 132. Notes on numerical fluid mechanics and multidisciplinary design. Springer, Cham, pp 663–673. [https://doi.org/10.1007/978-3-319-27279-5\\_58](https://doi.org/10.1007/978-3-319-27279-5_58)
- Schwermer T, Gardner AD, Raffel M (2019) A novel experiment to understand the dynamic stall phenomenon in rotor axial flight. *J Am Helicopter Soc* 64(1):1–11. <https://doi.org/10.4050/JAHS.64.012004>
- Spalart PR, Rumsey CL (2007) Effective inflow conditions for turbulence models in aerodynamic calculations. *AIAA J* 45(10):2544–2553. <https://doi.org/10.2514/1.29373>
- Stanfield JH, Betts CJ (1995) Transition detection technique in use in the DRA Bedford wind tunnels. In: Proceedings of the 7th international symposium on flow visualization, Seattle, WA, USA, pp 929–934
- Vieira BAO, Kinzel MP, Maughmer MD (2017) CFD hover prediction including boundary-layer transition. In: 55th AIAA aerospace sciences meeting, Grapevine, TX, USA. <https://doi.org/10.2514/6.2017-1665>
- Vuillet A, Allongue M, Philippe JJ, Desopper A (1989) Performance and aerodynamic development of the super puma MK II main rotor with new SPP 8 blade tip design. In: 15th European rotorcraft forum, Amsterdam, Holland
- Walker GJ, Gostelow JP (1990) Effects of adverse pressure gradients on the nature and length of boundary layer transition. *J Turbomach* 112(2):196–205. <https://doi.org/10.1115/1.2927633>
- Weiss A, Gardner AD, Klein C, Raffel M (2017) Boundary-layer transition measurements on Mach-scaled helicopter rotor blades in climb. *CEAS Aeronaut J* 8(4):613–623. <https://doi.org/10.1007/s13272-017-0263-2>
- Weiss A, Gardner AD, Schwermer T, Klein C, Raffel M (2018) On the effect of rotational forces on rotor blade boundary-layer transition. *AIAA J* 57(1):252–266. <https://doi.org/10.2514/1.J057036>
- Wolf CC, Mertens C, Gardner AD, Dollinger C, Fischer A (2019) Optimization of differential infrared thermography for unsteady boundary layer transition measurement. *Exp Fluids* 60(19):1–13. <https://doi.org/10.1007/s00348-018-2667-0>
- Zhao Q, Wang J, Sheng C (2018) Numerical simulations and comparisons of PSP and S-76 rotors in hover. In: 56th AIAA aerospace sciences meeting, Kissimmee, FL, USA. <https://doi.org/10.2514/6.2018-1780>

**Publisher's Note** Springer Nature remains neutral with regard to jurisdictional claims in published maps and institutional affiliations.